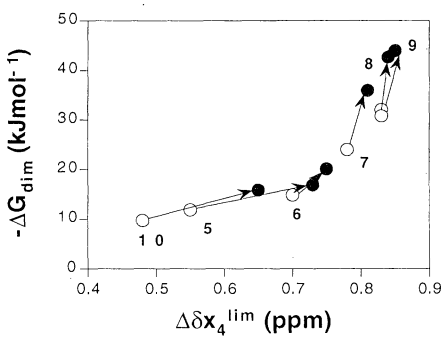

Fig. 3. Combined plot of $-\Delta G_{dim}$ versus $\Delta\delta x_4^{lim}$ for free (open circles) and ligand-bound (filled circles) antibiotics **5** to **10**. For any one antibiotic, arrows represent changes occurring upon ligand binding.

tors) have loose structures before binding another protein (or in the specific case of a receptor, its natural ligand or a drug), then a portion of the binding affinity can be derived by tightening of the internal structures of the proteins in the resulting bound state. Given this possibility, the thermodynamic parameters for protein-protein associations, which are perplexing when analyzed in terms of interfacial interactions (*14*), can be seen to have much more complex origins. The findings may also be relevant to transmembrane signal transduction, most obviously when signal activation is coincident with receptor dimerization (*16*). Suppose a ligand binds strongly to the monomeric form of a receptor (which itself dimerizes weakly in the absence of a ligand) and binds cooperatively to the dimeric form of the receptor. Such a system is well constituted to produce a tightening of the structure of the receptor at its dimer interface and hence to assist in ligand-induced changes in geometry (even without obvious allosteric changes) at points remote from ligand binding.

REFERENCES AND NOTES

1. L. Stryer, *Biochemistry* (Freeman, New York, ed. 3, 1988), pp. 82, 154–156, 234, 240, 267, and 290.
2. D. H. Williams and M. S. Westwell, *Chem. Biol.* **3**, 6953 (1996).
3. D. H. Williams *et al.*, *J. Am. Chem. Soc.* **113**, 7020 (1991).
4. M. S. Searle *et al.*, *J. Chem. Soc. Perkin Trans. 1* **X**, 2781 (1996).
5. D. H. Williams *et al.*, *Chem. Biol.* **4**, 507 (1997).
6. J. P. Mackay *et al.*, *J. Am Chem. Soc.* **116**, 4581 (1994).
7. D. A. Beauregard, D. H. Williams, M. N. Gwynn, D. J. C. Knowles, *Antimicrob. Agents Chemother.* **39**, 781 (1995).
8. G. M. Sheldrick, E. Paulus, L. Vertesy, F. Hahn, *Acta Crystallogr. B* **51**, 89 (1995).
9. M. Schafer, T. R. Schneider, G. M. Sheldrick, *Structure* **4**, 1509 (1996).
10. P. J. Loll, A. E. Bevivino, B. D. Korty, P. H. Axelson, *J. Am. Chem. Soc.* **119**, 1516 (1997).
11. Before we recorded the NMR spectra, we lyophilized the glycopeptides twice from D_2O. All samples were prepared at pD 3.7 by adjustment with NaOD and CD_3CO_2D or DCl. All pD sample readings were measured with a Corning pH meter equipped with a combination glass electrode, and no corrections were made for an isotope effect. NMR spectra were recorded on Bruker DRX500 spectrometers, and one-dimensional (1D) and two-dimensional (2D) spectra were recorded with 16,000 or 8000 data points, respectively. Chemical shifts were measured with respect to internal sodium 3-trimethylsilyl-2,2,3,3-d_4-propionate at 300 K.
12. When monomer and dimer forms of the antibiotic were in fast exchange on the NMR time scale, δx_4 was typically followed in 1D spectra obtained over a concentration range (3 mM to 25 or 100 mM, depending on the antibiotic), and monomer and dimer chemical shifts obtained from curve fitting (Simplex least squares curve-fitting program) of the data were extrapolated to infinitely dilute and infinitely large concentrations. When peak overlap precluded the following of x_4 in 1D spectra, appropriate cross peaks in 2D spectra were used. In the cases in which a large dimerization constant resulted in slow exchange between the monomer and dimer on the NMR time scale, the x_4 signals from the monomer and dimer were correlated by preirradiation of the dimer signal, which resulted in a reduction in intensity of the signal due to x_4 in the monomer. For these antibiotics, appearance of the monomer signal could be followed in the 5 mM to 10 μM concentration range. The signal from x_4 in the monomer of **8** and **9** in the presence of di-*N*-acetyl-Lys-D-Ala-D-Ala could not be unambiguously assigned because of overlap with other signals in this region and the need for exceptionally low concentrations. The antibiotics **7**, **8**, and **9** have the same x_4 chemical shift for the monomer in the absence of di-*N*-acetyl-Lys-D-Ala-D-Ala [±0.02 parts per million (ppm)]. Considering the structural similarities of **7**, **8**, and **9**, it was considered reasonable to take the x_4 chemical shift for the monomers of **8** and **9** bound to di-*N*-acetyl-Lys-D-Ala-D-Ala as equal to that for **7**.
13. For antibiotics in which the monomer and dimer species were in fast exchange on the NMR time scale, the chemical shift of x_4 was followed at different antibiotic concentrations. From a plot of δx_4 versus concentration, the dimerization constants and limiting chemical shifts could be calculated (*6*). For antibiotics in which the monomer and dimer species were in slow exchange on the NMR time scale, at sufficiently low concentrations of antibiotic (10 to 100 μM), both monomer and dimer states were populated. Integration of appropriate peaks yielded K_{dim}. For **7**, **8**, and **9** in the presence of a ligand, K_{dim} was calculated from the rate of exchange (H → D) of the NH (w_5, see **11**) at the antibiotic interface (*6*) in comparison with the rate of exchange of this same NH in **7** to **9** (in the absence of a ligand), where K_{dim} is known.
14. For a recent review of protein-protein interactions, see W. E. Stites, *Chem. Rev.* **97**, 1233 (1997).
15. H.-J. Bohm, *J. Comput.-Aided Mol. Des.* **8**, 243 (1994).
16. F. Canals, *Biochemistry* **31**, 4501 (1992).

17. We thank BBSRC for financial support. A.J.M. gratefully acknowledges SmithKline Beecham, and M.S.W. thanks GlaxoWellcome Research and Lincoln College, Oxford. W.T. thanks the National Institute of Food Research, Ministry of Agriculture, Food, and Fisheries, Japan. Vancomycin, dechlorovancomycin (LY223997), chloroeremomycin (LY264826), and phenylbenzylchloroeremomycin (LY307599) were generously donated by Eli Lilly (Indianapolis, IN). Eremomycin was a gift from SmithKline Beecham (Harlow, UK).

20 January 1998; accepted 10 March 1998

Elucidation of the Chain Conformation in a Glassy Polyester, PET, by Two-Dimensional NMR

K. Schmidt-Rohr,* W. Hu, N. Zumbulyadis

The chain conformation of glassy poly(ethylene terephthalate) (PET) was characterized by two-dimensional double-quantum nuclear magnetic resonance (NMR). In amorphous carbon-13–labeled PET, the statistics of the O–$^{13}CH_2$–$^{13}CH_2$–O torsion angle were determined, on the basis of the distinct shapes of the two-dimensional NMR patterns of trans and gauche conformations. In crystalline PET, the trans content is 100 percent, but in the amorphous PET it is only 14 percent (±5 percent). An average gauche torsion angle of 70 degrees (±9 degrees) was obtained. Implications for materials properties of polyesters are discussed.

PET (Fig. 1) and related aromatic polyesters find widespread uses in tough, transparent packaging materials with good barrier properties, in polyester fibers, and in thin films for photographic or magnetic-tape applications, which represent multibillion dollar industries (*1*). The degree of crystallinity can vary from 0 to 50%, and noncrystalline glassy polyesters can be obtained by quenching from the melt, which produces transparent films. To understand details of the materials properties of amorphous and semicrystalline polyesters, such as glass-transition and melting temperatures, crystallization rates, maximum crystallinities, or gas-barrier properties, knowledge of their microscopic structure is required. Although the chemical and the crystal structures of PET are well known (Fig. 1) (*2–4*), the chain conformations in the amorphous state are poorly characterized. The torsion around the OC–CO single bond (Fig. 1) is the major degree of freedom; bond lengths

K. Schmidt-Rohr and W. Hu, Department of Polymer Science and Engineering, University of Massachusetts, Amherst, MA 01003, USA.
N. Zumbulyadis, Imaging Research and Advanced Development, Eastman Kodak Company, Rochester, NY 14650–2132, USA.

*To whom correspondence should be addressed.

and angles vary only slightly, and the sp^2-hybridized units are expected to be mostly coplanar. In the probability distribution of the OC–CO torsion angle ψ, maxima are expected near 180°, the trans conformation (*5*), and near ±60°, the gauche conformation (*2*, *3*, *5*).

Many groups have attempted to estimate the positions and populations of the trans and gauche conformations for PET (*2*, *3*, *6*–*9*), which are important parameters in rotational-isomeric-state (RIS) models (*2*, *3*). Calculations unconstrained by experimental data tend to produce relatively high trans populations (*6*, *7*), which predict a larger extension of PET chains in solution than is observed experimentally (*2*, *3*). Therefore, the choice of RIS parameters is usually guided by dipole moments or *J* couplings of low–molar-mass model compounds (*2*, *3*, *6*–*10*). Nevertheless, these procedures have failed to produce a consistent parameter set. The predicted trans populations range from 6 to 36%, and the ψ of the gauche state has been treated as an adjustable parameter, ranging between 40° and 80° (*8*). In addition, most of the data used in the analyses were derived from ethers, polyethers, or esters of low molar mass, rather than from the polyesters themselves. The transfer of these results to PET is questionable because of the substantial effects of solvent or long-range chemical structure (*9*).

Vibrational spectroscopy is sensitive to molecular conformation, but quantification is often difficult because of severe peak overlap, poorly known oscillator strengths, and the overly localized or delocalized nature of many normal modes. The assignment of bands to trans and gauche conformations is mostly empirical. For amorphous PET, trans contents of 5 (*11*), 7 (*12*), 15 (*13*), 21 (*14*), and 14 or 24% (*15*) have been estimated by extrapolation in a series of samples with varying degrees of crystallinity. The average torsion angle of the gauche state (ψ_g) has so far not been determined experimentally. It is also uncertain whether the maxima in the ψ distribution are sharp enough to warrant the description by RIS models, which disregard the potential scatter of ψ values. This issue has recently been raised by the results of fully atomistic simulations including intermolecular interactions, which show very broad ψ distributions (*16*).

Solid-state nuclear magnetic resonance (NMR) can be used to quantify local structure and dynamics in both ordered and disordered solid polymers (*17*–*22*). Through anisotropic nuclear-spin interactions and the resulting angle-dependent NMR frequencies, the nuclei act as local probes of segmental orientations in space, with the strong external magnetic field $\mathbf{B}_0$ serving as the reference axis (*17*). In two-dimensional (2D) double-quantum NMR experiments that were introduced recently (*20*, *21*), the torsion angle between two bonded ^{13}C-labeled segments is determined by measuring their relative orientation, with the angle-dependent chemical-shift frequencies ω_a and ω_b of the two ^{13}C nuclei as the orientational probes. In Fig. 1, ψ and the tensor orientations are indicated for PET with a doubly ^{13}C-labeled $O–^{13}CH_2–^{13}CH_2–O$ unit, produced by polycondensation of doubly ^{13}C-labeled ethylene glycol and unlabeled terephthalic acid.

In the version of the 2D double-quantum experiments (*21*) that yields the simplest spectra, INADEQUATE-type double-quantum evolution (*23*, *24*) is combined with complete dipolar decoupling during detection (*21*). In the resulting 2D spectrum, the chemical-shift sum frequency $\omega_a + \omega_b$ of the double-quantum coherence in the first spectral dimension ω_1 is correlated with the individual chemical shifts ω_a and ω_b of the nuclear magnetization observed in the second dimension ω_2. We obtained simulations of the resulting spectral patterns for trans (Fig. 2A) and gauche (Fig. 2B) conformations in PET (*22*) by numerical summation over the full range of segmental orientations. The 2D patterns (*25*), as well as their integral projections onto the double-quantum ω_1 axis shown on top (Fig. 2, A and B), were drastically different for the two types of conformations.

The experimental 2D double-quantum spectrum of $O–^{13}CH_2–^{13}CH_2–O$–labeled, 95% amorphous (*26*) PET (Fig. 2C) was dominated by the compact features of the gauche conformation, as shown in the simulation in Fig. 2B. Nevertheless, at low

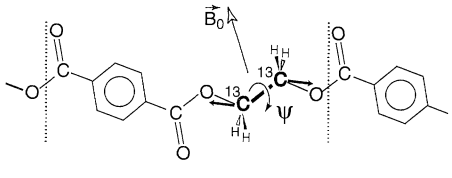

Fig. 1. Chemical structure of PET. The repeat unit is delimited by the dashed lines. For simplicity, the planar all-trans conformation is shown. The $O–^{13}CH_2–^{13}CH_2–O$ segment for which the conformational statistics were determined in this report is emphasized in bold. The bold arrows indicate the σ_{33} principal axes of the chemical-shift tensors. One arbitrary $\mathbf{B}_0$ field orientation is indicated.

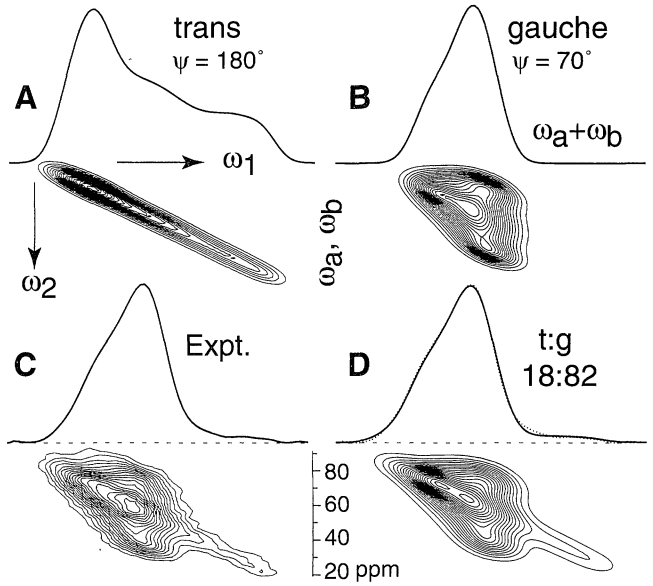

Fig. 2. Double-quantum NMR spectra of PET. (**A**) Simulated 2D spectrum of the trans conformation (ψ = 180°) (*5*). (**B**) Simulation of the gauche conformation (*5*), with ψ = ±70°. Projections onto the double-quantum ω_1 axis are shown at the top (*25*). (**C**) Experimental (Expt.) 2D double-quantum spectrum of 95% amorphous PET, with homonuclear $^{13}C–^{13}C$ decoupling in the detection period (*21*). Contour levels range from 4 to 100%. Note the straight ridge of the trans conformers observed at the right-hand side of the spectrum. (**D**) Corresponding simulation with a trans/gauche (t:g) ratio of 18/82. The experiments were performed on a Bruker (Billerica, Massachusetts) MSL-300 spectrometer (^{13}C: 74.75 MHz) in a Bruker probe head with a 5-mm coil, providing ^1H decoupling B_1 fields with $\gamma B_1/2\pi$ = 120 kHz (where γ is the magnetogyric ratio) and ^{13}C 90° pulse lengths of 2.8 μs. Recycle delay, 5 s; contact time of cross polarization, 0.5 ms; 44 time-data points in the evolution time t_1, with increments of 20 μs. In the simulations, chemical-shift parameters for the crystalline trans conformers were principal values of 87, 76, and 22 parts per million (ppm) and polar coordinates α = 40° and β = 113° of the C–C bond in the chemical-shift principal-axes system (PAS) (*22*). For the amorphous trans, 89, 79, and 23 ppm and the same tensor orientation were used. For the gauche conformers, principal values of 85, 73, and 33 ppm were estimated from 1D and 2D powder patterns; the PAS had an orientation similar to that of poly(ethylene oxide), with α = 90° and β = 126° (*22*, *34*). In these experiments and in ^2H NMR of deuterated PET (*33*), only restricted mobility of the methylene groups was detected. Our experimental double-quantum spectra show substantial correlated inhomogeneous broadening, possibly due to susceptibility effects. This broadening was taken into account in the simulations by convolution with a 2D Gaussian whose width along the (2ω, ω) line was nearly twice the width perpendicular to that line.

contour levels of 4 and 9% of the maximum intensity, the long straight ridge characteristic of the trans conformations is observed. Analysis of the intensities of the two components in the one-dimensional (1D) and 2D spectra shows that the trans conformations make up 13 to 23%. The best fit of the 1D double-quantum spectrum was obtained for a trans content of 18.5% and $\psi_g = 70.5°$ (Fig. 3). A spectral simulation with a trans fraction of 18% and $\psi_g = \pm 70°$ is shown in Fig. 2D. Taking into account the residual $5 \pm 2\%$ crystallinity of the sample (*26*), the trans content in the amorphous regions was thus determined as $14 \pm 5\%$ (*27*). Given the assumption that this trans/gauche ratio reflects the Boltzmann populations of the three minima in the intramolecular potential at the glass-transition temperature $T_g = 340$ K, the gauche energy is 3.3 ± 1.3 kJ/mol lower than that of the trans conformation. The relevant temperature of equilibration reflected in the conformational statistics is within the range of 340 ± 40 K, that is, between the sample storage temperature of 300 K and $T_g + 40$ K, where equilibration occurs on a submillisecond time scale during cooling; the variation of the trans content in this temperature range is only $\pm 1.5\%$.

The least squares fit procedure (Fig. 3C) yielded a ψ_g of $\pm 70°$ ($\pm 9°$), ruling out a gauche torsion angle of $\psi_g = \pm 40°$, as assumed in (*8*). Information on the width of the maxima in the ψ distribution can be obtained by comparing our experimental spectrum with simulations that use various widths of the peaks around 180° and ±70°. Results of a least squares analysis for full widths at half maximum (FWHM) of <5°, 50°, and 70° are shown in Fig. 3. The narrowest distribution provided the best fit, confirming that a RIS model (*2*, *3*) can provide a good approximation. Substantial deviations were seen to occur for half widths >50°.

To demonstrate how pronouncedly trans signals can show up experimentally, we crystallized the sample at 160°C for 2 hours, reaching a crystallinity of $30 \pm 3\%$ (*28*). The experimental 2D spectrum of this semicrystalline material (Fig. 4A) was dominated by the narrow straight ridge characteristic of the trans conformation in the crystallites. The minimum in the least squares fit was obtained for a trans/gauche ratio of 47/53 (±6) (*29*) and $\psi_g = 70°$ (Fig. 4B).

The difference in chain conformation between amorphous and crystalline regions of PET observed here and in the vibrational spectroscopy studies (*11*–*15*) rules out models of a locally ordered bundled or nanocrystalline glassy state of PET. It is fully consistent with Flory's prediction of unperturbed random conformational statistics and chain dimensions in the melt (*2*). It is exceptional that the chains in the crystallites of PET have a higher intramolecular energy than in the amorphous state. In most other polymers, the conformation in the crystals is close to the minimum-energy conformation of the isolated chain (*30*).

The low trans probability in the melt may be the primary reason for the relatively low crystallization rate of PET (*31*), which allows it to be easily quenched into the amorphous state. According to Strobl, the rate-limiting step in crystallization is the straightening of the chains on being incorporated into the growing crystal (*32*). Our results imply that this transition from the mostly gauche conformation in the melt to the required all-trans conformation in the crystal is accompanied by not only an entropic but also a substantial enthalpic penalty, which increases the barrier to crystallization. Support for our hypothesis that the conformation in the methylene region determines the crystallization rate is provided by the substantially higher crystallization rate observed for poly(butylene terephthalate) (PBT) (*31*), a polyester whose chemical structure closely resembles that of PET except for two additional methylene groups in each repeat unit. Because other factors affecting crystallization, such as the difference between melting and glass-transition temperatures, are similar for PET and PBT, the conformational difference in the methylene regions provides the best known explanation for their different crystallization rates.

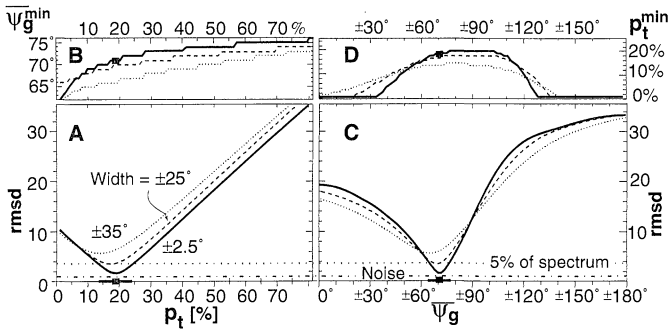

Fig. 3. Determination of trans content p_t and central ψ_g in 95% amorphous PET. In a least squares fit, the root-mean-square deviation (rmsd) between the experimental 1D double-quantum spectrum of Fig. 2C and calculated double-quantum spectra was minimized simultaneously as a function of p_t and ψ_g. Root-mean-square deviation curves for different FWHM (<5°, solid curve; 50°, dashed curve; 70°, dotted curve) of the peaks in the ψ distribution are compared in (A) and in (C). For each curve, the width of the spectral line broadening was adjusted to minimize the rmsd. The rmsd minimum position was found to be independent of the line broadening over a wide range. The rmsd is given in multiples of the random-noise value, indicated by the dash-dotted line. The straight dotted line indicates the level of 5% fractional rmsd (relative to the rms value of the experimental spectrum at 100%), which can be regarded as the maximum acceptable deviation between simulation and experiment. (**A**) Plot of minimum (min) rmsd for a given p_t [occurring at various ψ_g positions, as plotted in (B)]. (**B**) Plot of the ψ_g position of the minimum rmsd, for the trans content p_t given on the *x* axis. The variation of ψ_g with the trans content is seen to be smaller than ±3° near the global rmsd minimum, which occurs at $p_t = 18.5\%$ and $\psi_g = 70.5°$. The quality of this fit can be judged in Fig. 2D. (**C**) Minimum rmsd for a given ψ_g. (**D**) Value of p_t at which the minimum rmsd of (C) occurs, as a function of ψ_g. Near the global minimum, the variation of the trans content is less than −4%/+1%.

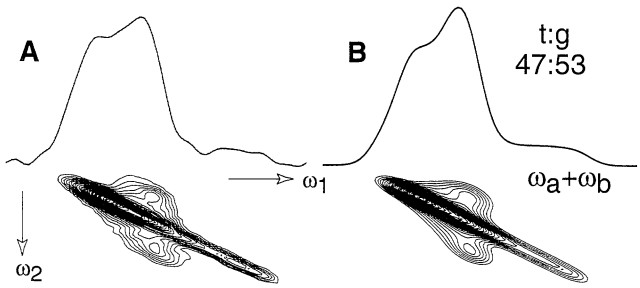

Fig. 4. Double-quantum NMR spectrum of semicrystalline PET. (**A**) Spectrum of a 30 ± 3% crystalline PET sample. (**B**) Corresponding simulation with a trans/gauche ratio of 47/53. The intrinsic spectral resolution is somewhat higher than in Fig. 2, C and D.

REFERENCES AND NOTES

1. *Chemical Week*, 19 June 1996, p. 38.
2. P. J. Flory, *Statistical Mechanics of Chain Molecules* (Wiley-Interscience, New York, 1969), pp. 190–192.
3. W. L. Mattice and U. W. Suter, *Conformational Theory of Large Molecules* (Wiley, New York, 1994), pp. 234–237.
4. R. de P. Daubeny, C. W. Bunn, C. J. Brown, *Proc. R. Soc. London Ser. A* **226**, 531 (1954).
5. Trans is also known as (fully staggered) anti or antiperiplanar, and gauche is also known as synclinal. The trans conformation of PET is shown in Fig. 1.
6. E. Riande and J. Guzman, *J. Polym. Sci. Polym. Phys. Ed.* **23**, 1235 (1985).
7. I. Bahar and W. L. Mattice, *J. Chem. Phys.* **90**, 6783 (1989).
8. F. Mendicuti, M. M. Rodrigo, M. P. Tarazona, E. Saiz,

Macromolecules **23**, 1139 (1990).
9. J. San Roman, J. Guzman, E. Riande, J. Santoro, M. Rico, *ibid.* **15**, 609 (1982).
10. P. J. Flory and J. E. Mark, *Makromol. Chem.* **75**, 11 (1964); A. Abe, J. W. Kennedy, P. J. Flory, *J. Polym. Sci. Polym. Phys. Ed.* **14**, 1337 (1976); A. Abe and J. E. Mark, *J. Am. Chem. Soc.* **98**, 6468 (1976); A. Abe, K. Tasaki, J. E. Mark, *Polym. J.* **17**, 883 (1985).
11. A. Ajji, J. Guèvremont, K. C. Cole, M. M. Dumoulin, *Polymer* **37**, 3707 (1996).
12. X. Yang, F. Long, D. Shen, R. Qian, *ibid.* **32**, 125 (1991).
13. J. C. Rodriguez-Cabello, L. Quintanilla, J. M. Pastor, *J. Raman Spectrosc.* **25**, 335 (1994).
14. M. Yazdanian, I. M. Ward, H. Brody, *Polymer* **26**, 1779 (1985); A. Cunningham, I. M. Ward, H. A. Willis, V. Zichy, *ibid.* **15**, 749 (1974).
15. S. B. Lin and J. L. Koenig, *J. Polym. Sci. Polym. Phys. Ed.* **20**, 2277 (1982); J. Liu and J. L. Koenig, *Anal. Chem.* **59**, 2609 (1987).
16. R. F. Rapold, U. W. Suter, D. N. Theodorou, *Macromol. Theory Simul.* **3**, 19 (1994).
17. K. Schmidt-Rohr and H. W. Spiess, *Multidimensional Solid-State NMR and Polymers* (Academic Press, London, 1994).
18. G. Dabbagh, D. P. Weliky, R. Tycko, *Macromolecules* **27**, 6138 (1994).
19. P. Robyr *et al.*, *Mol. Phys.* **84**, 995 (1995); M. Tomaselli *et al.*, *ibid.* **89**, 1663 (1996).
20. K. Schmidt-Rohr, *Macromolecules* **29**, 3975 (1996).
21. ———, *J. Magn. Reson.*, in press.
22. ———, W. Hu, N. Zumbulyadis, in preparation.
23. A. Bax, R. Freeman, S. P. Kempsell, *J. Am. Chem. Soc.* **102**, 4849 (1980); A. Bax, R. Freeman, T. Frankiell, M. H. Levitt, *J. Magn. Reson.* **43**, 478 (1981); R. R. Ernst, G. Bodenhausen, A. Wokaun, *Nuclear Magnetic Resonance in One and Two Dimensions* (Oxford Univ. Press, Oxford, 1987).
24. T. Nakai and C. A. McDowell, *Mol. Phys.* **79**, 965 (1993).
25. The 2D spectra were rotated by 90° from the traditional representation to simplify the comparison of the intensity patterns along the double-quantum dimension.
26. To make the PET sample amorphous, we quenched it from the clear melt into liquid nitrogen. The residual crystallinity was 5 ± 2% according to the following measurements. Wide-angle x-ray scattering (WAXS) showed only an amorphous halo (crystallinity < 8%). From the density $\rho = 1.34(4 \pm 2)$ g/cm^3 measured by flotation in a series of salt solutions, the crystallinity was estimated as 4.5 ± 1.5%, on the basis of amorphous and crystalline densities of $\rho_a = 1.33(6 \pm 2)$ g/cm^3 and $\rho_c = 1.5(1 \pm 2)$ g/cm^3, respectively. Thermal analysis (difference between crystallization and melting peak areas, with a heat of fusion Δh_f = 140 ± 20 J/g) yielded 8 ± 4% crystallinity. Cross-polarization–magic-angle spinning (CP-MAS) ^{13}C NMR showed no separate crystalline peak; selection of the long ^{13}C longitudinal relaxation time T_1 components yielded 3 ± 2.5% crystallinity.
27. The trans fraction of the amorphous phase was obtained as (18.5% − 5%)/0.95 = 14%.
28. The sample obtained by crystallizing the amorphous PET at 160°C for 2 hours had a crystallinity of 32 ± 4% by thermal analysis and 28 ± 4% by CP-MAS NMR. WAXS showed strong crystalline reflections.
29. In the semicrystalline sample, relatively fast relaxation of the spin-locked ^{1}H magnetization of the amorphous phase was observed. With a rotating-frame spin-lattice relaxation time $T_{1\rho}$ of ~4 ms, the signal from the amorphous regions observed in the ^{13}C spectrum was attenuated by 0.88 during the cross-polarization spin lock of 0.5 ms. Thus, the 47/53 (±6) trans/gauche ratio found in the spectrum had to be corrected slightly to 44/56 (±6).
30. G. Natta and P. Corradini, *Nuovo Cimento Suppl. Ser. X* **XV**, 13 (1960).
31. D. C. Clagett, in *Encyclopedia of Polymer Science & Engineering*, H. F. Mark *et al.*, Eds. (Wiley, New York, 1989), vol. 6, pp. 114–115; J. Y. Jadhav and S. W. Kantor, in *ibid.*, vol. 12, p. 219.
32. G. Strobl, *The Physics of Polymers* (Springer-Verlag, New York, 1996), pp. 169–172.
33. S. Roeber and H. G. Zachmann, *Polymer* **33**, 2061 (1992).
34. K. Schmidt-Rohr, M. Wilhelm, A. Johansson, H. W. Spiess, *Magn. Reson. Chem.* **31**, 352 (1993).
35. Generous financial support for K.S.-R. by a Beckman Young Investigator Award is gratefully acknowledged. Partial support was also provided by the NSF Materials Research Science and Engineering Center and by NSF grant DMR-9703916. K.S.-R. thanks M. Hong for stimulating discussions on data quantification.

23 October 1997; accepted 10 March 1998

Effect of Substrate Strain on Adsorption

M. Gsell, P. Jakob, D. Menzel*

Direct evidence for the effect of local strain at a surface on the bonding strength for adsorbates is presented. Scanning tunneling microscopy revealed that adsorbed oxygen atoms on Ru(0001) surfaces are located preferentially on top of nanometer-size protrusions above subsurface argon bubbles, where tensile strain prevails, and are depleted around their rim in regions of compression, relative to the flat surface. Such effects can be considered as the reverse of adsorbate-induced strain, and their direct local demonstration can be used to test theoretical predictions.

In recent years structure determinations of surfaces and adsorbate layers have become sufficiently exact to give detailed information about the structural changes at the surface compared with the bulk, and about the adsorption-induced shifts of substrate atoms (*1*). Even for surfaces without major rearrangement of the surface atoms (reconstruction), both lateral and normal (to the surface) shifts are found, which can vary considerably from one substrate surface atom to the next. Eventually the interatomic arrangements must join on to those of the undisturbed substrate lattice, so that considerable stress can exist in the near-surface region. Quite often these forces—which are, of course, the result of the changed bonding situation—lead to a major reconstruction, releasing some of the residual stress. Adsorption of gases causes complicated shifts of surface atoms (*1*, *2*), which should further modify these lateral and normal forces and interact with them.

On a more macroscopic scale, the developing stress can be made visible by tracing the deformation of thin crystals upon gas adsorption, either optically (*3*) or in a capacitive way (*4*). Adsorption introduces stress in the surface region of a crystal that can vary strongly on an atomic scale, causing displacements of substrate atoms from their original positions (strain), and the stress may also have an average component on a larger scale, allowing detection by macroscopic probes. On a mesoscopic scale the developing stress influences the morphology of bimetallic layers and local ordering (*5*).

Physik-Department E 20, Technische Universität München, D-85747 Garching, Germany.

*To whom correspondence should be addressed. E-mail: menzel@e20.physik.tu-muenchen.de

One would then expect that strain within the surface region of a crystal introduced by external influences should change its adsorptive properties. Theoretically, a dependence of the strength of adsorbate bonding on the surface lattice constant is expected, which should be quantifiable with large-scale, total-energy calculations. Obtaining direct experimental proof is not easy, however. For example, it is difficult to discern whether the changed adsorption strength at surface steps is primarily due to the (unquestionably existing) local strain or rather to additional electronic effects such as the electron redistribution under the strong electric field at a step. Applying an external force to bend the sample seems like the most promising way to study the intrinsic effect of strain on the adsorption properties of various gases. However, such macroscopically applied external forces will inevitably lead to the creation of numerous dislocations that form easily, especially for metals. On the other hand, external forces that are sufficiently weak not to be relaxed in this way will probably have only small effects, which would be difficult to discern. Another possibility, the formation of pseudomorphic substrate layers with crystal lattice constants different from the normal surfaces, has been used by Kampshoff *et al.* (*6*). The observed frequency shifts of the internal C-O stretch mode of adsorbed CO were interpreted by them in terms of lattice strain. However, effects other than the direct geometry change, especially structural defects in the bimetallic layers or dynamic frequency shifts, may also have affected their vibrational line positions.

We chose a way to create local strain fields and combined it with local imaging with the scanning tunneling microscope (STM). Local strain was produced on a